

# CONTENTS

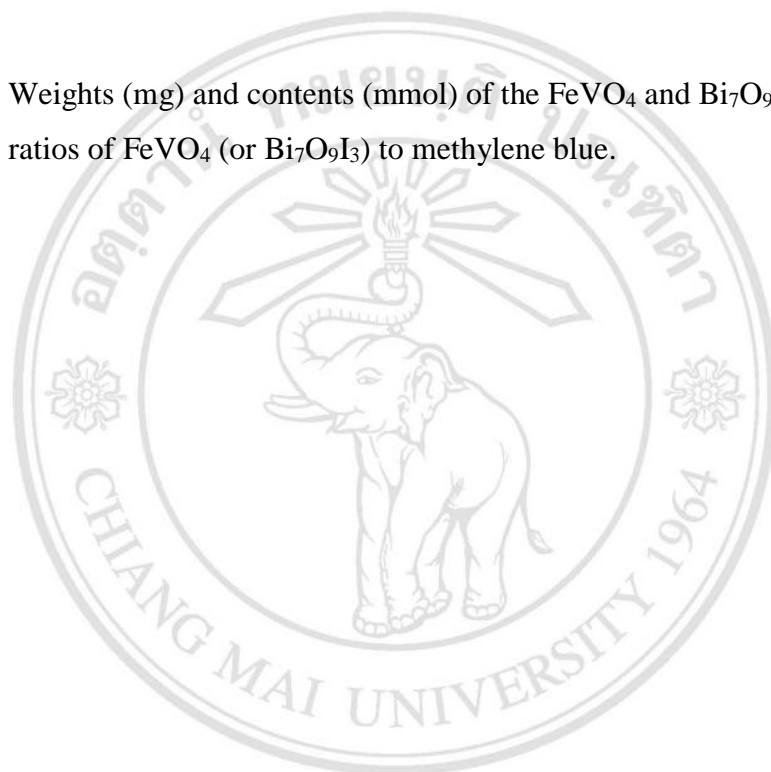
	Page
Acknowledgement	c
Abstract in Thai	d
Abstract in English	f
Lis of Tables	j
List of Figures	k
Chapter 1	1
1.1 Photocatalysis	1
1.2 Bismuth oxyhalide	4
1.3 Bismuth-rich strategy	5
1.4 Semiconductor-Semiconductor Heterostructures	7
1.5 Z-scheme heterojunction	8
1.6 Microwave synthesis	11
1.7 Literatures review	19
1.8 Research objectives	22
1.9 Usefulness of this research	22
Chapter 2	23
2.1 Chemical reagents and equipment	23
2.2 Synthesis method	25
2.3 Characterizations	26
Chapter 3	29

3.1	XRD analysis	29
3.2	FESEM, TEM, and EDX analyses	30
3.3	Optical properties	36
3.4	XPS analysis	37
3.5	Photocatalytic dye degradation	40
3.6	Electrochemical analysis	47
3.7	Photocatalytic mechanism	50
Chapter 4		52
4.1	Conclusion	52
4.2	Suggestions	53
References		54
Appendix		70
The Joint Committee for Powder Diffraction Standards (JCPDS) of $\text{FeVO}_4$		70
The Joint Committee for Powder Diffraction Standards (JCPDS) of $\text{BiOI}$		75
Curriculum Vitae		79

ลิขสิทธิ์มหาวิทยาลัยเชียงใหม่  
 Copyright© by Chiang Mai University  
 All rights reserved

## LIST OF TABLES

		Page
Table 1	Dielectric constant and tangent delta for some solvents (values determined at 2.45 GHz and room temperature).	16
Table 2	Weights (mg) and contents (mmol) of the $\text{FeVO}_4$ and $\text{Bi}_7\text{O}_9\text{I}_3$ , and mole ratios of $\text{FeVO}_4$ (or $\text{Bi}_7\text{O}_9\text{I}_3$ ) to methylene blue.	42



ลิขสิทธิ์มหาวิทยาลัยเชียงใหม่  
Copyright© by Chiang Mai University  
All rights reserved

## LIST OF FIGURES

	Page
Figure 1.1	Reactive oxygen species generated in the photocatalytic reduction and oxidation steps of oxygen and water. 3
Figure 1.2	Primary steps in the photocatalytic mechanism (TiO <sub>2</sub> ). 3
Figure 1.3	Valence band and conduction band positions and the energy band gap of BiOX (X = Cl, Br, I). 4
Figure 1.4	(a) Crystal structure of BiOCl. (b) Model showing the direction of the internal electric field in BiOCl with (001) exposed facets. 5
Figure 1.5	(a-c) UV-vis diffuse reflection spectra (DRS) of Bi <sub>2</sub> O <sub>3</sub> and as-synthesized bismuth oxyhalides, the inset shows the plots of $(\alpha h\nu)^{1/2}$ vs. photon energy (hν), and (d) comparison of the band structures of Bi <sub>2</sub> O <sub>3</sub> and bismuth oxyhalides. 6
Figure 1.6	Degradation of bisphenol A (BPA) using blank (no catalyst), Bi <sub>2</sub> O <sub>3</sub> and as-synthesized bismuth oxyhalides as photocatalyst, respectively, under visible-light irradiation for 2 h; inset shows the chemical structure of BPA. 7
Figure 1.7	Diagrams illustrating the different types of heterojunctions. 8
Figure 1.8	(a) The discovery and evolution of Z-scheme photocatalysts. Schematic diagrams of (b) Traditional Z-scheme process (c) All-solid-state Z-scheme process, and (d) Direct Z-scheme process. 8
Figure 1.9	Schematic illustration of semiconductor-semiconductor with similar work function: (a) before contact, (b) after contact, (c) charge transfer process in Z-scheme mechanism, (d) charge transfer process in type-II mode, and (e) charge carrier recombination. 10
Figure 1.10	Schematic illustration of semiconductor-semiconductor with large different work function: (a) before contact, (b) after contact, (c) charge transfer process in type-II mode, and (d) charge transfer process in Z-scheme mechanism. 11

Figure 1.11	Electromagnetic wave.	11
Figure 1.12	Dipolar molecules which align itself with an applied electric field.	13
Figure 1.13	Charged particles in a heated substance following the applied electric field.	13
Figure 1.14	The temperature of ethanol and acetone. The upper curve is ethanol and the lower curve is acetone.	15
Figure 1.15	Sample heating; tradition heating (left) and microwave heating (right).	18
Figure 3.1	The XRD pattern of the $\text{FeVO}_4$ , $\text{Bi}_7\text{O}_9\text{I}_3$ , and $\text{FeVO}_4/\text{Bi}_7\text{O}_9\text{I}_3$ nanocomposites with different weight percentages of $\text{FeVO}_4$ .	30
Figure 3.2	FESEM images of the (a) $\text{FeVO}_4$ , (b) $\text{Bi}_7\text{O}_9\text{I}_3$ , and (c) 6.25%wt- $\text{FeVO}_4/\text{Bi}_7\text{O}_9\text{I}_3$ nanocomposite and (d) EDX spectrum of the 6.25%wt- $\text{FeVO}_4/\text{Bi}_7\text{O}_9\text{I}_3$ nanocomposite.	32
Figure 3.3	EDX spectrum and detailed chemical composition of the synthesized $\text{Bi}_7\text{O}_9\text{I}_3$ nanoparticles.	32
Figure 3.4	TEM and HRTEM images of $\text{FeVO}_4$ .	33
Figure 3.5	TEM and HRTEM images of $\text{Bi}_7\text{O}_9\text{I}_3$ .	34
Figure 3.6	The TEM image of the 6.25%wt- $\text{FeVO}_4/\text{Bi}_7\text{O}_9\text{I}_3$ nanocomposite. Upper and lower insets show the corresponding HRTEM images of $\text{FeVO}_4$ and $\text{Bi}_7\text{O}_9\text{I}_3$ parts, respectively.	35
Figure 3.7	EDX mapping of the 6.25%wt- $\text{FeVO}_4/\text{Bi}_7\text{O}_9\text{I}_3$ nanocomposite.	35
Figure 3.8	(a) UV-vis DRS of the $\text{FeVO}_4$ , $\text{Bi}_7\text{O}_9\text{I}_3$ , and 6.25%wt- $\text{FeVO}_4/\text{Bi}_7\text{O}_9\text{I}_3$ nanocomposites, and (b) PL spectrum of the 6.25%wt- $\text{FeVO}_4/\text{Bi}_7\text{O}_9\text{I}_3$ nanocomposite in comparison with the $\text{Bi}_7\text{O}_9\text{I}_3$ .	37
Figure 3.9	(a) Survey XPS spectra of the $\text{FeVO}_4$ , $\text{Bi}_7\text{O}_9\text{I}_3$ , and 6.25%wt- $\text{FeVO}_4/\text{Bi}_7\text{O}_9\text{I}_3$ nanocomposite; high-resolution spectra of (b) Bi 4f, (c) I 3d, (d) Fe 2p, (e) V 2p, and (f) O 1s, and (g) valence band XPS (VB XPS) spectra of $\text{FeVO}_4$ and $\text{Bi}_7\text{O}_9\text{I}_3$ .	39

Figure 3.10	(a) Decolorization efficiency (%) of the MB irradiated using LED lamp and (b) photocatalytic reaction kinetics of the degradation of MB. Photocatalysis condition: 200 mL of methylene blue ( $10 \text{ mgL}^{-1}$ or $0.0255 \text{ mmol}$ ) with 100 mg of the photocatalyst.	41
Figure 3.11	FESEM image of the 12.5% wt- $\text{FeVO}_4/\text{Bi}_7\text{O}_9\text{I}_3$ powder.	43
Figure 3.12	(a) Decolorization efficiency (%) of RhB and MO compared to that of MB, (b) the reusing assessment of the 6.25% wt- $\text{FeVO}_4/\text{Bi}_7\text{O}_9\text{I}_3$ photocatalyst for photocatalytic degradation of $10 \text{ mgL}^{-1}$ of RhB, (c) the effect of initial concentration on photocatalytic degradation of RhB, and (d) the trapping experiments of active species in the photocatalytic reaction in the presence of the 6.25% wt- $\text{FeVO}_4/\text{Bi}_7\text{O}_9\text{I}_3$ photocatalyst.	45
Figure 3.13	Photocatalytic reaction kinetics of the degradation of the (a) $10 \text{ mgL}^{-1}$ of MB, RhB, and MO solutions and (b) different initial concentrations of RhB solution.	46
Figure 3.14	The UV-vis absorption spectra of the (a) RhB, (b) MO, and (c) MB.	46
Figure 3.15	Linear sweep voltammograms of the $\text{Bi}_7\text{O}_9\text{I}_3$ and the 6.25% wt- $\text{FeVO}_4/\text{Bi}_7\text{O}_9\text{I}_3$ photoanodes in dark and under light illumination.	48
Figure 3.16	Mott-Schottky plots for the as-synthesized (a) $\text{Bi}_7\text{O}_9\text{I}_3$ and (b) $\text{FeVO}_4$ .	49
Figure 3.17	EIS plots of $\text{FeVO}_4$ , $\text{Bi}_7\text{O}_9\text{I}_3$ , and 6.25% wt- $\text{FeVO}_4/\text{Bi}_7\text{O}_9\text{I}_3$ .	49
Figure 3.18	Schematic diagrams of formation of p-n junction and proposed charge separation process in the $\text{FeVO}_4/\text{Bi}_7\text{O}_9\text{I}_3$ heterostructure under visible-light irradiation.	51